



**Journal of Engineering
Sciences Assiut University
Faculty of Engineering**

Vol. 49, No. 2

March 2021

PP. 215 - 247



**FLEXURAL BEHAVIOR OF RC CONTINUOUS T-BEAMS
REINFORCED WITH HYBRID CFRP/ STEEL BARS:
EXPERIMENTAL AND NUMERICAL STUDY**

Hesham M. Diab¹, Tarek Abdelaleem², Mohamed M.M. Rashwan³

¹*Civil Eng. Dept., Faculty of Eng., Assiut University, Assiut 71515, Egypt
Email: diab@aun.edu.eg*

²*Civil Eng. Dept., Faculty of Eng., Assiut University, Assiut 71515, Egypt
Email: tarekabelaleem@aun.edu.eg*

³*Civil Eng. Dept., Faculty of Eng., Assiut University, Assiut 71515, Egypt*

Received 15 January 2021; Revised 16 March 2021; Accepted 17 March 2021

Abstract

This study presents experimental and numerical investigations to understand the response and failure of hybrid RC continuous T-beams reinforced in flexure by both Carbon Fiber Reinforced Polymer (CFRP) bars and steel bars at sagging and hogging regions. Three RC continuous T-beams were constructed experimentally and studied to discuss three parameters which are the type of reinforcement material, the relation between sagging and hogging reinforcement, and the moment redistribution. The control beam was reinforced with steel rebars that have been designed to fail in flexure. The second beam was reinforced with hybrid CFRP/ steel bars at the sagging and hogging regions. The sagging region of the third one was reinforced with steel bars while the hogging region was reinforced with CFRP bars. All critical sections at the tested specimens are designed to have the same axial stiffness for the reinforcement bars. Experimental results revealed that the moment redistribution ratio and mode of failure depend on the type of reinforcement bars and using the hybrid bars at both critical regions helped to control the serviceability limits of the beams. This study also suggests and validates a 3D

numerical model to simulate the performance and failure of hybrid reinforced RC continuous T-beams using the finite element (FE) software “ANSYS”. The results agreed with the experimental observations that indicated significant effect of the type of reinforcement material at sagging and hogging regions on the failure mode and the redistribution of the moment of the RC continuous beams.

Keywords: Continuous beams, Hybrid reinforcement, CFRP bars, Moment redistribution, Serviceability, FEA, Numerical.

1. Introduction

The steel bars are effective reinforcement for concrete elements owing to their elasticity modulus, elastoplastic properties, and ultimate strength. Corrosion of steel bars, in contrast, is a crucial challenge resulting from the cracking of concrete covers or poor construction processes, particularly in aggressive environments such as marine facilities or those continuously exposed to moisture. In the past few decades, fiber-reinforced polymers (FRPs) have become a solution to compensate the steel bars in strengthening concrete structures. Nevertheless, their brittleness is the main downside of the FRP bars. FRP materials have linear elastic behavior before failure, which negatively affects and restricts the RC structure's inelastic response [1]. Most research and design codes have suggested the design of these elements as over-reinforcement elements to ensure better ductility and to prevent sudden failure of the FRP structures. Over and above, the lack of ductility for FRP bars are recognized in comparison with steel bars by their low elasticity modulus, especially the GFRP bars [2]. Consequently, the FRP reinforced concrete (FRP-RC) structures suffer from excessive deflections and large cracks that impair its serviceability. In this case, the design of FRP-RC structures should be governed by their limit state of serviceability, rather than their ultimate limit state [3]. CFRP-bars, by contrast, offers the reinforced element little deflection values with a weak ductility behavior. Therefore, the concept of combining steel bars with FRP bars (hybrid system) in the reinforcement concrete structures appears to be a practical approach to solve the problems of ductility and serviceability of FRP-RC structures [4, 5].

Many forms of research have proposed several approaches to boost ductility, including the hybridization of various types of fibrous material [6, 7] and the integration of steel reinforcement with composite materials for producing rebars with internal steel and an external FRP [8-10]. Because of the high cost and difficulty of the manufacturing process, these methods were not practical to be executed in the construction industry. More practical solutions have been proposed to improve the ductility, stiffness, and serviceability of FRP-RC structures by using the combination of FRP and steel bars [11-13, 1].

Such a hybrid reinforcement can offer high stiffness and ductility in concrete beams and expanded load-carrying capability relative to conventional reinforcement [14]. Although the literature reveals some research on simply supported beams reinforced with hybrid FRP and steel rebars [11, 12, 15], few types of study of such design initiatives have been undertaken to examine the structural nature and failure modes of multi-span continuous hybrid reinforced concrete beams that vary significantly from those of simply supported ones. Concrete continuous beams are thus not well reflected by statically determinate specimens that were examined in previous studies. The characteristics of the redistribution moment and the changes in the curvature of the beam from sagging to hogging do not exist in simply supported beams. In addition, most RC concrete structures are in practice continuous members of multi-spans. Mohamed and Ashour [14] investigated the amount of longitudinal GFRP, steel reinforcements and area of steel bars to GFRP bars of RC continuous beams. They concluded that the increase of the GFRP reinforcement ratio at the maximum moment zones simultaneously increased the load capacity with brittle behavior and the situation was reversed as the steel reinforcing ratio improved. Recently, Diab et al. [16, 17] studied the behavior of RC continuous T-beam strengthened with NSM FRP or NSM steel bars at hogging and sagging regions. They concluded that the serviceability and the moment redistribution depended on the type of NSM strengthening bars and on the strengthened region. All strengthened beams failed after yielding the un-strengthened regions with separation of the end anchorage of the NSM bars at strengthened region.

Based on the above background, it can be found that research of RC continuous beams reinforced with hybrid steel and CFRP rebars is limited. Consequently, this research provides a study on the behavior of the RC continuous T-beams reinforced with hybrid steel and CFRP

rebars at hogging and sagging regions. This study takes into consideration the relation between the type of reinforcement at sagging and hogging regions. The axial stiffness of longitudinal hybrid reinforcement sections is kept constant for all beams. The use of finite element analysis (FEA) has been the preferred method to study the behavior of RC continuous beams reinforced with hybrid steel and CFRP rebars (for economic reasons). For this purpose, three RC continuous T-beams reinforced with hybrid steel and CFRP rebars at sagging or hogging were tested to investigate their behavior, particularly in flexural rigidity, moment redistribution, and the failure mode. In addition, 3D FE analyses based on ANSYS/standard software were conducted to provide analytical estimation of the flexural capacity and moment redistribution of the RC continuous T-beams reinforced with hybrid steel and CFRP rebars.

Table 1: Reinforcement Details and compressive strengths of Test Specimens.

Beam specimen	bottom reinforcement at mid-span							Main top reinforcement at central support							f_{cu} N/mm ²
	A_s mm ²	A_f mm ²	EA *10 ⁶ (N/mm ²)	ρ_s %	ρ_f %	ρ_b %	ρ_{eff} %	A_s mm ²	A_f mm ²	EA *10 ⁶ (N/mm ²)	ρ_s %	ρ_f %	ρ_b %	ρ_{eff} %	
BS	226	—	47.46	0.43	—	2.13	0.43	226	—	47.46	0.43	—	2.13	0.43	28.0
BH	157	113	47.50	0.30	0.22	0.067	0.27	157	113	47.50	0.30	0.22	0.067	0.27	27.5
BCH	226	—	47.46	0.43	—	2.13	0.43	—	339	50.17	—	0.65	0.077	0.65	29.0

Table 2: Mechanical Properties of the Reinforcing Bars.

Bar size	Bar diameter (mm)	Bar Area (mm ²)	Modulus of elasticity (GPa)	Yield Strength (MPa)	Yield strain ($\mu\epsilon$)	Tensile Strength (MPa)	Ultimate strain ($\mu\epsilon$)
8	7.6	45.36	200	360	2800	482	72820
10	10	78.5	196	509	3010	665.80	65000
12	12	113	210	522	3280	640.60	58543

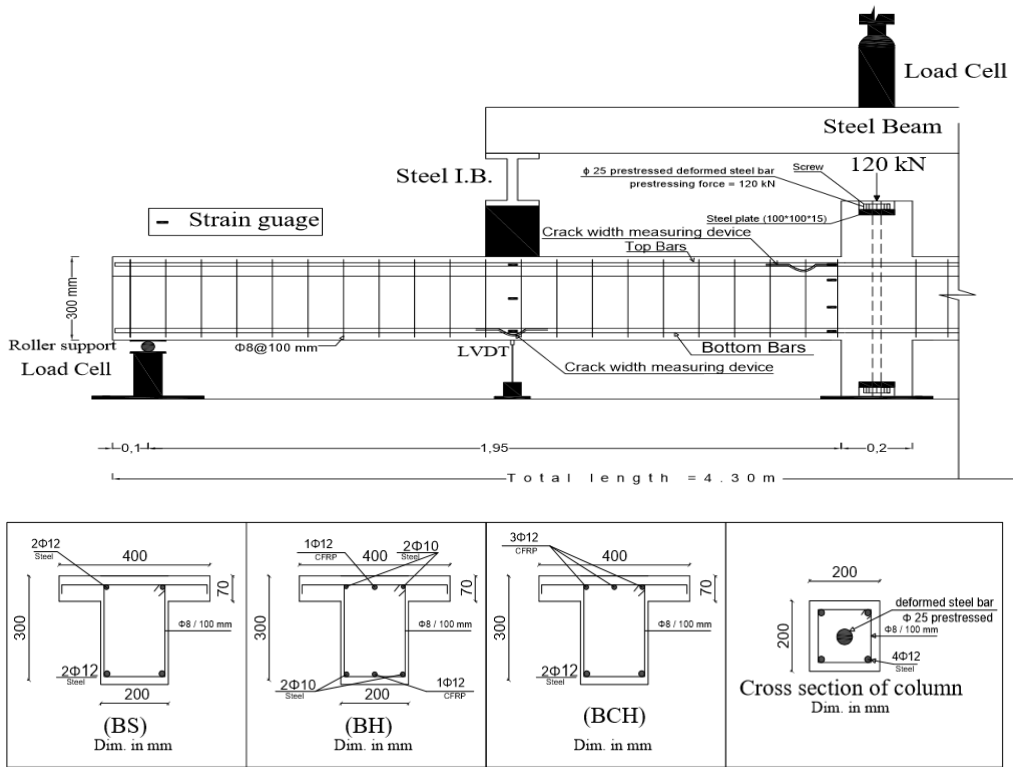


Figure 1: Series of tested beams and the middle column.



Figure 2: Arrangement of the reinforcement for the hybrid beams.

2. Test Specimens

Three RC continuous T-beams (BS, BH, and BCH) were designed with the same initial flexural stiffness as shown in Table 1. The dimensions and the reinforcement of the tested beams are shown in figures (1 and 2). The mechanical properties of reinforcing bars are shown in Table 2. All

the tested beams are 4300 mm in length with two equal spans, each of 2150 mm, the cross-sectional area is $200 \times 230 \text{ mm}^2$ for the web and $400 \times 70 \text{ mm}^2$ for the flange. The designed strength grade of RC concrete beams was C25 and the average compressive strength of the three concrete cubes ($150 \times 150 \times 150 \text{ mm}^3$) is shown in Table 1. The continuous RC steel beam (BS) has two high tensile steel bars, (12 mm) diameter, at the maximum moment regions, sagging and hogging. The beam BS was designed to achieve a ductile failure. This may be accomplished by reinforcing the hogging and sagging sections with reinforcement ratio lower than the balanced reinforcement ratio ρ_{bs} . The corresponding rectangular stress block of concrete recommended by buildings department [18], was used for estimate ρ_{bs} , as illustrated in Eq. (2).

A_s = area of the steel bars, steel percentage in tension:

$$\rho_s = \frac{A_s}{bd}, \dots\dots\dots(1)$$

balanced reinforcement ratio for pure steel section:

$$\rho_{bs} = 0.85\beta_1 \frac{f_{cu}}{f_y} \frac{E_s \epsilon_{cu}}{f_y + E_s \epsilon_{cu}} \dots\dots\dots(2)$$

Where β_1 is the ratio between the depth of the equivalent rectangular concrete stress block and that of the neutral axis, $\epsilon_{cu} = 0.0035$ which is the extreme concrete strain in compression in conjunction with f_{cu} , and f_y is the yield strength of the main reinforcement.

Only CFRP reinforcement was used in this study between the accessible FRP bars. The mid-span and the central support regions at the beam BH were reinforced with two high tensile steel bars, (10 mm) diameter, and one CFRP bars, C12 (12 mm) diameter. The BH hybrid beam was built on the premise that the failure mode is controlled by the steel yielding prior to the concrete crushing or rupture of the CFRP bars. While the beam BCH was reinforced at the sagging region like the beam BS, and with three CFRP bars, (12) mm diameter, at the hogging region. In pure FRP-RC section, the balanced FRP reinforcement ratio, ρ_{bf} , is a situation in which the rupture of FRP reinforcement occurs at once with the concrete crushing, which results in the beam failure. Considering the balanced reinforcement ratio of both steel and pure FRP sections, a balanced reinforcement ratio for hybrid FRP-RC sections is proposed as the condition that concrete crushing in compression zone and the rupture of FRP reinforcement occurs concurrently. The equivalent rectangular

stress block of concrete recommended in ACI 318-19 [19] is used to calculate the balanced reinforcement ratio for both pure and hybrid FRP-RC sections. The balanced reinforcement ratio for pure FRP-RC section, ρ_{bf} , is shown in the following equation according to ACI 440.1R-15 [20].

A_f = area of the CFRP bars, FRP percentage in tension:

$$\rho_f = \frac{A_f}{bd}, \dots\dots\dots(3)$$

The balanced reinforcement ratio for pure FRP-RC section:

$$\rho_{bf} = 0.85\beta_1 \frac{f_c'}{f_{fu}} \frac{E_f \epsilon_c}{f_{fu} + E_f \epsilon_c} \dots\dots\dots(4)$$

Where β_1 is the ratio between the depth of the equivalent rectangular concrete stress block and that of the neutral axis, $\epsilon_c = 0.003$ which is the extreme concrete strain in compression in conjunction with f_c' , and f_{fu} is the tensile strength of the FRP rebars.

In this way, the type of tensile reinforcement was considerably varying, resulting in multiple forms of failure, some of which were ductile (steel yielding) and some of which were brittle (concrete crushing), as recommended by the provisions of ACI-318-19 [19] and recommended by Qin et al. [21]. For all specimens, the effective reinforcement ratio, ρ_{eff} , is calculated from the following equation:

$$\rho_{eff} = \rho_f + \frac{f_y}{f_{fu}} \cdot \rho_s \dots\dots\dots(5)$$

defined including both steel in tension and CFRP bars areas.

The thickness of the concrete cover to the center of the bottom and top reinforcement was 40 mm. All-tested beams were also reinforced with 8 mm diameter closed steel stirrups spaced at 100 mm along the beam's spans. More details about the description of the experimental beams can be found elsewhere [22].

3. Experimental Results and Discussion

3.1 Failure modes, cracking patterns and crack width

The experimental tests of three continuous RC T-beams up to failure with different effective reinforcement ratios and the same flexural

stiffness led to three different types of failure depending on the type of reinforcement as shown in figures (4-7) and Table 3.



Figure 3: Experimental setup.

Table 3: Experimental results at cracking, service yield and ultimate loads of test specimens.

Beam Specimen	P_{cr}		P_y		kN.m $M_{y(exp.)}$		P_u	$M_{u(exp.)}$ kN.m		Failure mode
	Hogging region	Sagging region	Hogging region	Sagging region	Hogging region	Sagging region		Hogging region	Sagging region	
	BS	81.25	71	195	202	42.26		33.3	251.25	
BH	80	68.5	207.5	222	31.55	38.51	304.5	40.96	58.03	shear failure
BCH	102.5	68.25	—	221.81	48.32*	29.78	330.75	97.31	36.02	Yielding of steel followed by rupture of FRP bars

*At yielding of sagging steel reinforcement

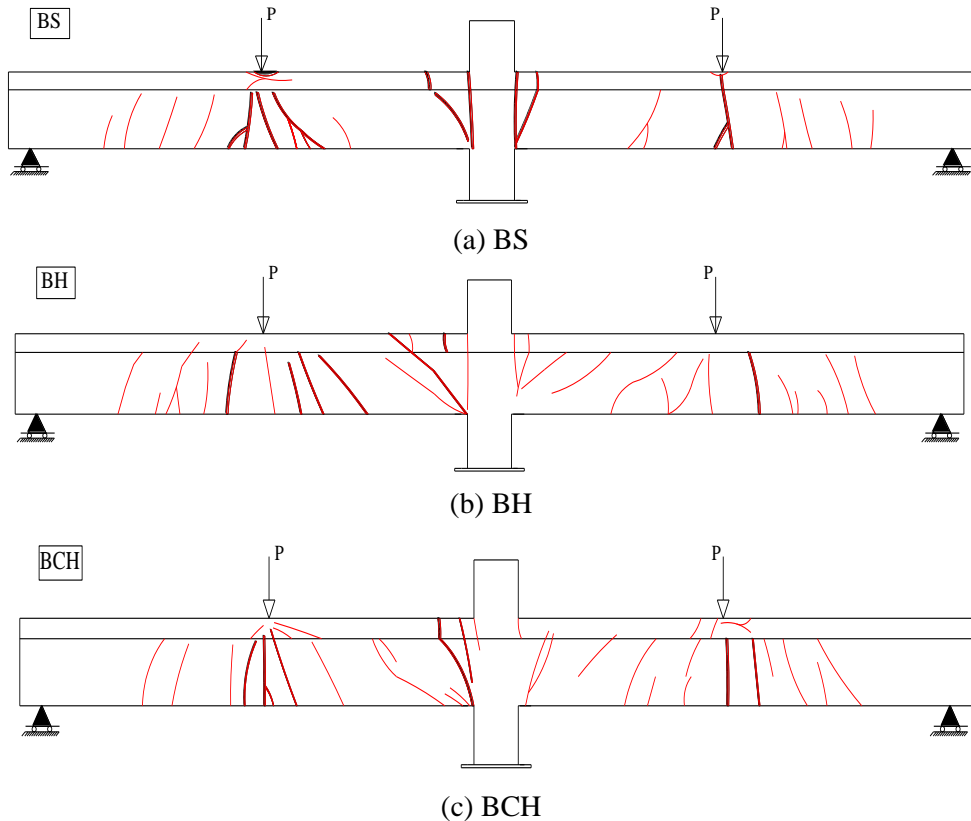


Figure 4: Cracking patterns of the tested continuous beams.

Mode 1: Conventional ductile flexural failure

The beam, BS, showed fewer cracks with larger spacing compared to the others. The first concrete cracking was at 71 kN at the sagging moment region. At load 81.25 kN, the hogging moment region began to crack while the cracks passed through the flange at load 90 kN. Most of the cracks concentrated at the maximum moment regions and spread to the compression zones with increasing their width. Before yielding of steel, the shear cracks began to appear at the shear spans, these cracks propagated and distributed regularly along two-beam spans. The closest crack to the end supports was at load 230 kN and with 420 mm distance, this shear crack was formed after yielding of steel. The distances between the cracks were from (150- 200) mm. The cracks width increased dramatically after yielding of steel while the load capacity slowly increased until the beam failure. The observed mode of failure was yielding of the top and bottom steel bars at the maximum moment regions at loads 195 kN and 202 kN respectively, which equal 78% and

80% of the ultimate load, and so the yield of the main steel allowed plastic hinges to develop at the central support and at the mid-spans of the beam, which increased the deformation, followed by concrete crushing at the ultimate load. See Figures (4 and 5).



(a) General view



(b) Middle support region.



(c) Top view at middle



(d) Mid-span region.

Figure 5: Failure modes of beam BS

(a) General view



(b) Middle support region.



(c) Top view at middle support



(d) Mid-span region.

Figure 6: Failure modes of beam BH.

Mode 2: Shear failure

The reinforced concrete continuous hybrid beam, BH, generally, cracks were observed along the beam spans. The crack initiation was at 68.5 and 80 kN at maximum positive and negative regions respectively. At

110 kN, flexural cracks began to spread far from the maximum moment regions. The distance between the cracks is roughly the same distance between the beam BS cracks, taking into account the increase in the number of cracks for the beam BH and with lower cracks width. This hybrid beam characterized by small cracks width even after yielding of steel. As shown in figures (6), the central support region cracks extended and spread to a 600 mm distance from the column, these cracks propagated to the web as inclined cracks between the column and the mid-span sections, it started at load 170 kN and extended through the beam depth at load 230 kN. This beam did not show the expected ductile behavior and failed in shear due to a sudden diagonal crack at a distance of 500 mm from the column.



(a) General view



(b) Middle support region



(c) Top view at middle support



(d) Mid-span region

Figure 7: Failure modes of beam BCH.

Mode 3: Yielding of steel followed by rapture of FRP bars

For the beam, BCH, the cracks began at loads 68.28 kN and 102.5kN at the critical sections. The cracks extended through the flange at load 180 kN, while the total web depth cracked at the sagging region at load 130 kN. The cracks width and distance along the beam span was similar to that of the beam BS, nevertheless, the negative moment zone was characterized by a small width of cracks until the yield load (222 kN). Two shapes of cracks, parallel and perpendicular to the flange width, extended up to a distance 800 mm from the column. The mode of failure was yielding of the main steel reinforcement at the sagging region with increase the width of the cracks, and then rapture of the CFRP bars in

the hogging region followed by a diagonal crack through the beam thickness with angle 70° , as shown in figure (7).

Figures (8 and 9). show the total load versus flexural crack width at the both critical sections. On the whole, the crack width in the critical sections was affected by varying the reinforcement bars type, especially after yielding of steel. The hogging moment regions showed a clear smaller crack width compared to that of the sagging moment regions, where the crack widths at the positive moment regions were almost equal twice of those in the hogging moment regions. For the steel beam, the crack widths were 0.46 mm at both critical regions before yielding of steel, these widths developed dramatically to reach 3.4 mm and 6.2 mm at the ultimate load for the hogging and the sagging regions respectively. But reinforcing with the CFRP bars in the hybrid beam BH continued to control the crack widths up to failure, where the crack width increased from 0.31 mm to 1.28 mm at the sagging region when the loading varied from 200 kN to 304.5 kN at the sagging region. This indicates that the existence of CFRP bars in the hybrid beam restricted the quick and deep distribution of cracks seen in RC steel beam (BS). The flexural crack width behavior for the beam BCH was similar to those at the beam BS, because of the symmetry of the bottom reinforcement. But the beam BCH characterized by higher loads at the same crack width after yielding of steel and less cracking widths at the hogging region in comparison with the steel beam.

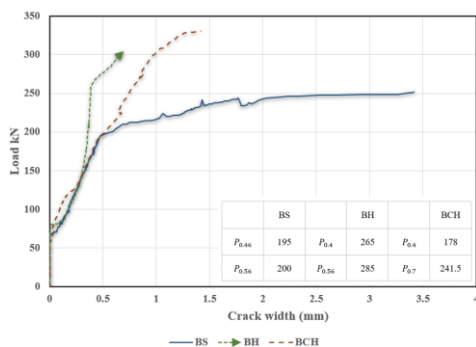


Figure 8: Total applied load versus flexural crack width at the hogging region

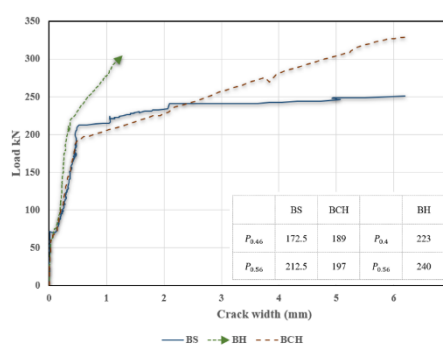


Figure 9: Total applied load versus flexural crack width at the sagging region

For beam BS, the maximum crack width should not exceed 0.46-0.56 mm [19]. Crack width in the sections reinforced with FRP bars at aggressive environmental conditions should not exceed 0.4 mm, and 0.7mm for other members [20], the maximum crack width limits are slightly larger than that of RC beam. Because of the good corrosion resistance of the FRP, the serviceability limit requirements for the FRP section can be used at the hogging region for the beam BCH and both critical regions for the beam BH. As shown in figures, it is evident that all beams at service load (67 % ultimate load) in the hogging area did not reach the permissible crack width limit. Moreover, beam BCH exceeded the limits specified for steel reinforcement at the sagging moment region.

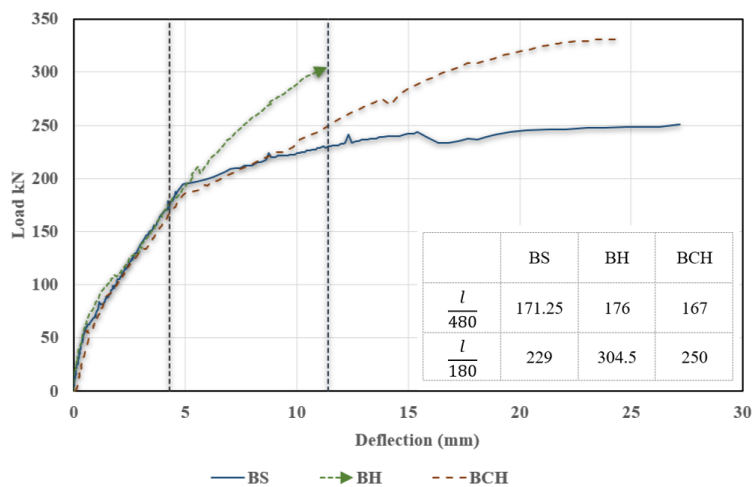


Figure 10: Load-mid span deflection curves of specimens.

3.2 The Load-Displacement Curve

The load mid-span displacement curves for the specimens are presented in figure (10), and the corresponding characteristics values can be seen in Table 4, where the Δ_y is the deflection of the specimens when the longitudinal reinforcement began to yield, Δ_u is the maximum deflection for the specimens, the loads ($P_{L/480}$ and $P_{L/180}$) occurred at mid-span deflections ($L/480$ and $L/180$), respectively. All beams showed linear load-deflection behavior up to the cracking load, this is ascribed to the linear elastic characteristics of concrete, CFRP bars, in addition to steel bars before reaching the yielding point. After the linear stage reached its limit by concrete cracking, the beam stiffness is controlled by

reinforcing bars which play a significant role in post cracking stage. It could be noticed that the load-displacement curve of the beam BS showed three different regions as follow; pre-cracking, post cracking and yielding of steel. After - yielding of steel for beam BS, it showed lower stiffness and subsequently higher mid-span deflections, as it could be seen in figure (10). The hybrid beam BH, - presented a bilinear curve in both uncracked and cracked stages and it exhibited lower deflection than the others. The decrease at the slope of the load-displacement curve was not respectable even after the yielding of sagging steel due to the CFRP bar at the positive moment region. The beam BCH, which was reinforced with CFRP bars at only the hogging region, it showed load-deflection curve similar to the BS with higher load capacity and the stiffness of this beam lies between the others, especially after the yielding of sagging steel. Overall, the type of the sagging reinforcement is a crucial factor in the beam deflection value, while the hogging reinforcement plays an influential role in the beam ultimate load.

Table 4: Deflection test results.

Beam Specimen	Δ_y (mm)		Δ_u (mm)	$\Delta_u/\Delta_y(\text{sagging})$	$P_{L/480}$ (kN)	$P_{L/180}$ (kN)	stiffness%		E_y (kN. mm)	E_u (kN. mm)	μ_E
	hogging	sagging					At L/480	At L/180			
BS	4.92	6.3	27.21	4.32	171.25	229	—	—	480	1055	2.20
BH	5.75	6.25	11.361	1.82	176	304.5	+3.14	+72.4	495	1226	2.48
BCH	—	8.80	24.38	2.77	167	250	-4.04	+15.77	657	2233	3.40

Table 4 shows the relative stiffness of the hybrid beams compared to that of the beam (BS) at the service loads ($\Delta = L/ 480$ and $L/ 180$), using Eq. (6) [8]. To understand the impact of post-yield rigidity, the energy ductility coefficient was taken as another index [23] that can be observed in Eq. (7).

$$\text{Stiffness \%} = \frac{\Delta_{BS} - \Delta_B}{\Delta_B} * 100 \dots\dots\dots(6)$$

$$\mu_E = \frac{E_u}{E_y} \dots\dots\dots(7)$$

Where; Δ_{BS} is the RC steel beam (BS) deflection, and Δ_B is the deflection of beam BH or BCH. The yield energy E_y is the triangular area and the ultimate energy E_u is the total area under the load-deflection curve.

From Table 4, as expected, the steel-reinforced continuous beam, BS, exhibited the highest stiffness among the others, owing to the higher modulus of elasticity of steel than the CFRP bars before yielding of steel. With the increase in external load, the yield was resulted at mid-span for the BS beam, and led to a significant decrease in beam flexural stiffness. Oppositely, because of the elastic and brittle nature of CFRP reinforcement, the stiffness of the hybrid beams reduced slightly compared to the beam BS after yielding of the bottom reinforcement. So, the CFRP bars played an essential assignment in resisting load after yielding of steel. Besides, the beams with steel bars at the sagging region demonstrated ductile behavior before failure, attributable to yielding characteristics of steel bars. Where the energy ductility coefficient is a better performance index than the displacement ductility coefficient as it appropriately takes into consideration the higher ultimate strength brought by FRP. The beam BCH had a better performance than the others, where the reinforcement with CFRP at the hogging region helped to improve the ultimate load after the yield load. Moreover, the sagging reinforcement preserved the beam ductility.

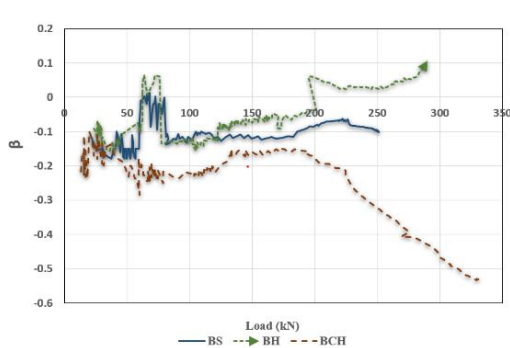


Figure 11: Load-moment redistribution ratio at the hogging region for all tested beams

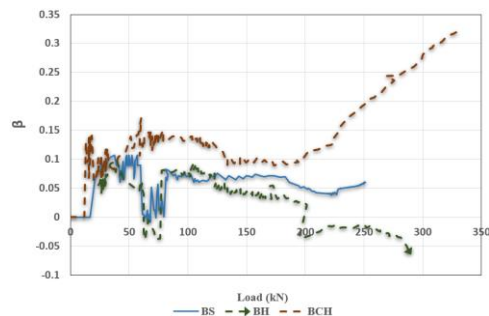


Fig. 12. Load-moment redistribution ratio at the sagging region for all tested beams

3.3 Moment redistribution

The moment redistribution ratio (β) given in Table 5 was calculated for the sagging and the hogging bending moment at mid-span and at the central support at any stage of the loading. The ratio was calculated by Eq. (8):

$$\beta = \frac{M_e - M_{ex}}{M_e} * 100 \dots\dots\dots(8)$$

Where; M_e , is the value of the moment at central support and mid-span is based on the elastic analysis and M_{ex} is the experimental value of bending moment at any stage of loading.

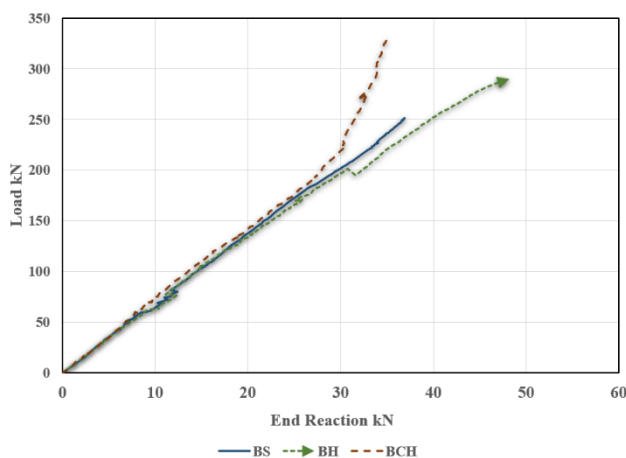
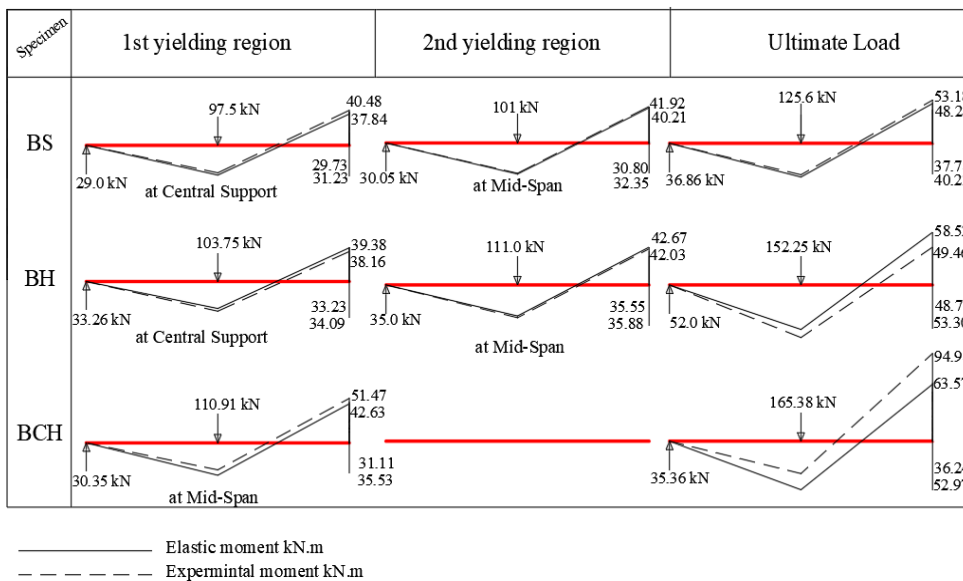


Fig. 13. Load-end reactions relationship for all tested beams

At Table 5, figures (11, 12 and 13), it can be seen that the redistribution of the moment from the sagging to the hogging regions and the end reactions values varied according to the type of the reinforcement bars despite their equal axial stiffness. In the case of beam BS, where the reinforcement steel areas were equal at the critical sections, the shape of the cross-section was the influencing factor in the moment redistribution and the central loaded column helped to increase the hogging region flexural stiffness. After the cracking at the sagging region, the internal forces were repositioned from mid-span region to negative moment section. At the yield loads, the modulus of elasticity for the steel bars at the hogging region began to decrease with an increase in the crack width. For these reasons the flexural rigidity of the negative moment section

began to weaken. Thus, the rate of redistribution of the internal forces had reduced until yielding of steel at the sagging region. With the increase of the external loads after the yield loads, the plastic hinge started to form at the mid-span region and this was followed by the formation of the plastic hinge in the hogging region. Subsequently, at the ultimate load, the experimental moment at the mid-span was less than the elastic moment, and this explains the slight increase in the end reaction from the yield to the ultimate loads.

Table 5: End support reaction, moments at yield, ultimate loads and moment redistribution of the tested beams.



As a result of reinforcing by hybrid bars at both critical regions (beam BH) with the same axial stiffness, the moment redistribution was from the mid-span region to the hogging region like the beam BS. After yielding of the top steel, the moment redistribution was from negative to positive section with a sudden increase in the moment redistribution, then its value gradually decreased after the bottom steel yielding. Beyond that loads, the support reaction distribution is suddenly shifted as more loads transferred to the end supports leaving the middle support with less load. Due to the continuity of the load transfer to the end supports, beam BH had the largest reaction value at these supports. On the other side, the end supports had the less reactions value at the beam BCH where the reinforcement at the middle support had uniform axial

stiffness, which controlled the crack widths in that region, unlike the ductile behavior at the sagging region, as the cracks formed in the maximum positive moment regions and the flexural rigidity weakened, the internal forces transferred from the sagging area to the hogging area.

4. Predicted Failure Loads

The expected failure load P_{pre} of the continuous concrete beams would be obtained as explained below [14].

For a fully ductile beam, the expected load capacity is based on a yield of the main steel reinforcement followed by concrete crushing after the formation of the plastic hinge. Therefore, Eq. (9) could calculate P_{pre} on each span:

$$P_{pre} = \frac{2}{L} (M_{uh} + 2M_{us}) \dots\dots\dots(9)$$

Where: M_{uh} and M_{us} , are the maximum moment capacities at the central support and mid-span regions, respectively, and L is the span length of concrete member.

For CFRP reinforcement, for each span, the flexural ultimate load is the lower load that allows the moment capacity to be reached at either middle support. ($P_{pre} = \frac{M_{uh}}{0.188L}$) or mid-span ($P_{pre} = \frac{M_{us}}{0.156L}$) section.

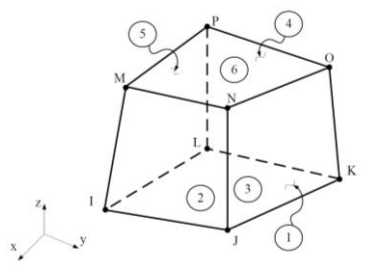


Figure 13: Element SOLID 65 (reproduced from user manual ANSYS 2018).

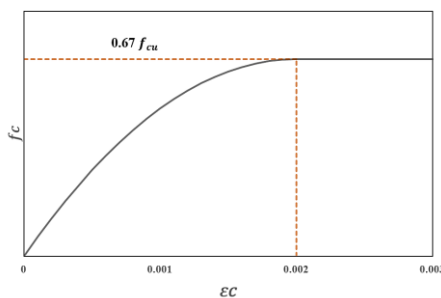


Figure 14: Simplified uniaxial stress-strain concrete curve.

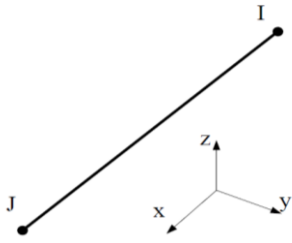


Figure 15: LINK180 finite element (reproduced from user manual ANSYS 2018).

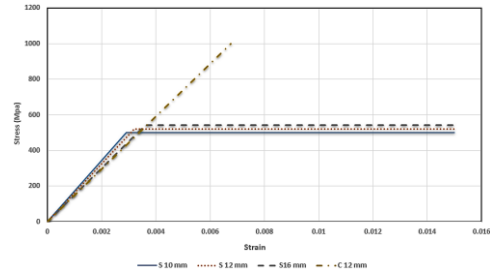


Figure 16: Stress-strain relationship of reinforcement materials used in finite element modeling

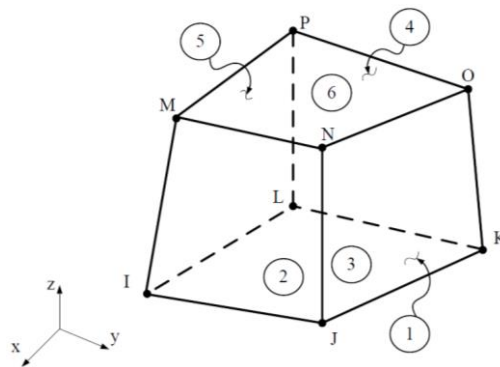


Figure 17: Element SOLID45 (reproduced from user manual ANSYS 2018).

Table 6: Experimental and predicted ultimate loads of the tested beams.

Beam specimen	Experimental failure load (p_{exp})	Predicted failure load (p_{pre})		p_{exp}/p_{pre}	
		p_1	p_2	p_{exp}/p_1	p_{exp}/p_2
BS	251.25	213	170	1.18	1.48
BH	304.5	328	282	0.93	1.08
BCH	330.75	299.5	223	1.10	1.48

As shown in Table 6, calculating the failure loads based on fully ductile material is more accurate in the case of beams BS and BCH, while the flexural loads capacity which were calculated based on brittle elastic materials or loads based on fully ductile material, are suitable in the case of reinforcing with hybrid bars at two critical regions, taking into account using $\frac{A_f}{A_s} \%$ at this hybrid beam.

5. Finite Element (FE) Modeling

The numerical analysis research in this study is listed in this section. To simulate the flexural performance of RC continuous beams reinforced with steel bars BS or hybrid bars, a non-linear finite element (FE) model was constructed. In this method, the finite element analysis software package available for academia, ANSYS (ANSYS 2018.1) [24], was used. To check the accuracy of the established FE model, the experimental results existing in the earlier analysis were used. The steps for constructing the FE model are discussed in detail, as well as the elements used in modeling, properties of the used materials and boundary conditions. Furthermore, the various assumptions made in the finite element modeling process, including meshing, concrete constitutive models and the solution approach used, are also mentioned.

5.1 Material properties and elements types

In this analysis, concrete was modeled using solid elements of three-dimensional eight-nodes. For the modeling of concrete, the solid element, SOLID 65, was used. The key aspect of this element is the ability to allow for material nonlinearity. This element will take into account cracking, plastic deformation and crushing in three perpendicular directions, as shown in figure (13). In order to properly model concrete, SOLID 65 elements require linear isotropic and multi-linear isotropic material properties [24]. In this study, the Poisson's ratio was assumed to be 0.2 and the modulus of elasticity of concrete (E_c) was calculated based on the following equation:

$$E_c = 4500\sqrt{f_c} \dots\dots\dots(10)$$

Where: f_c is the maximum cylinder compressive strength.

Normal strength concrete's stress-strain relationship in compression usually consists of two parts; an ascending branch and a descending branch. However, in ANSYS software, the use of the ideal stress-strain curve with the descending branch contributes to problems with convergence. The descending branch of the concrete material model in ANSYS was, therefore, ignored in this review, as recommended in previous studies [25, 26]. The following equations were used to model the ascending branch of the multi-linear isotropic stress-strain curve for the concrete [27].

$$f_c = \begin{cases} f_c' \left(\left(\frac{2\varepsilon_c}{0.002} \right) - \left(\frac{\varepsilon_c}{0.002} \right)^2 \right) & \text{for } \varepsilon_c < 0.002 \dots\dots\dots (11) \\ f_c' & \text{for } 0.002 \leq \varepsilon_c \leq 0.0035 \dots\dots\dots (12) \end{cases}$$

Where: f_c = stress (in MPa) at any strain; ε_c = strain at stress f ;

Figure (14) represents the uniaxial stress-strain concrete curve. The first point is defined to be at stress equals to 30% of the ultimate compressive strength of the concrete, considering the pre-defined Young`s modulus and satisfying Hooke`s Law;

$$E = \frac{\sigma}{\varepsilon} \dots\dots\dots(13)$$

There are different constants that should be defined (ANSYS 2018), typical shear transfer coefficients differ from 0.0 to 1.0, with a smooth crack (absolute absence of shear transfer) representing 0.0 and a rough crack representing 10 (no loss of shear transfer). Based on the experimental specimens, the shear transfer coefficients for open and closed cracks were taken as 0.3 and 0.5. The stress of uniaxial cracking was based on the rupture modulus and was determined using the following equation.

$$f_r = 0.62\sqrt{f_c'} \dots\dots\dots(14)$$

In the concrete model, the remainder of the variables are essentially parameters to describe the concrete biaxial compressive strength. Since the ANSYS program can describe the failure surface with at least two constants, f_r and f_c' , these variables have been left to default.

In this study, the reinforcement materials have been modelled as truss elements with one node at each end. To that end, the LINK180 finite element was used. There are three degrees of freedom in the end nodes of this element, translation in the nodal directions of x, y and z. This element`s behavior is able to simulate nonlinearity and plastic deformations. Figure (15) shows the geometry and nodes of this element. The LINK180 element requires linear isotropic and bi-linear isotropic material properties to be described to properly model steel reinforcement. The same element was specified instead with linear-elastic material properties in order to model FRP reinforcement. For steel

reinforcement and FRP, the Poisson ratio was assumed to be 0.3 and 0.2, respectively. As discussed earlier, the modulus of elasticity for reinforcement materials was obtained experimentally. Figure (16) shows the stress-strain relationship for the reinforcement material used in this study. The steel bearing plates used to distribute concentrated stresses at supports and loading points were also modeled. For this reason, the SOLID45 finite element was used. There are eight nodes in this element, each with three degrees of freedom. In figure (17), the geometry and nodes of element SOLID45 are shown. The steel bearing plates were constructed as a linear-elastic material with a 200 Gpa and 0.3 Poisson ratio.

5.2 ANSYS model geometry and boundary conditions

In geometry, loading and internal reinforcement, all tested beams are symmetric in the longitudinal direction around the middle support position. The cross-section of the beams tested is also symmetrical to the vertical axis that passes through center of gravity of the cross-section. Just one-quarter of the beam was modeled in ANSYS, using two-axis of symmetry. The computational time and the appropriate storage desk space were significantly reduced by this method, which allowed the use of a finer mesh in modeling. To reflect the effect of continuity, the boundary conditions have been defined at the symmetry axes, see figure (18). The horizontal translation was restrained at the middle support in the longitudinal direction and at the cross-section symmetry axis in the transverse direction. To simulate a roller at the end support and a hinge at the middle support, the boundary conditions at the external supports were set. This was done by limiting only vertical translations at the end support, thus restricting both vertical and horizontal translations at the central support. In addition, translations to external support in the out-of-plane direction were also avoided.

The column was subjected to a constant axial load equal to 120 kN, as it was subjected to before the experimental test, in order to understand the effect of axial forces on the nonlinear analysis. This load was added to the column in the form of surface pressure. Documented experimental studies confirm that the application of the column axial load increases to some extent the confinement effect of the beam-column joint region and contributes to an improvement in the joint's shear strength [28], as shown in figure (18).

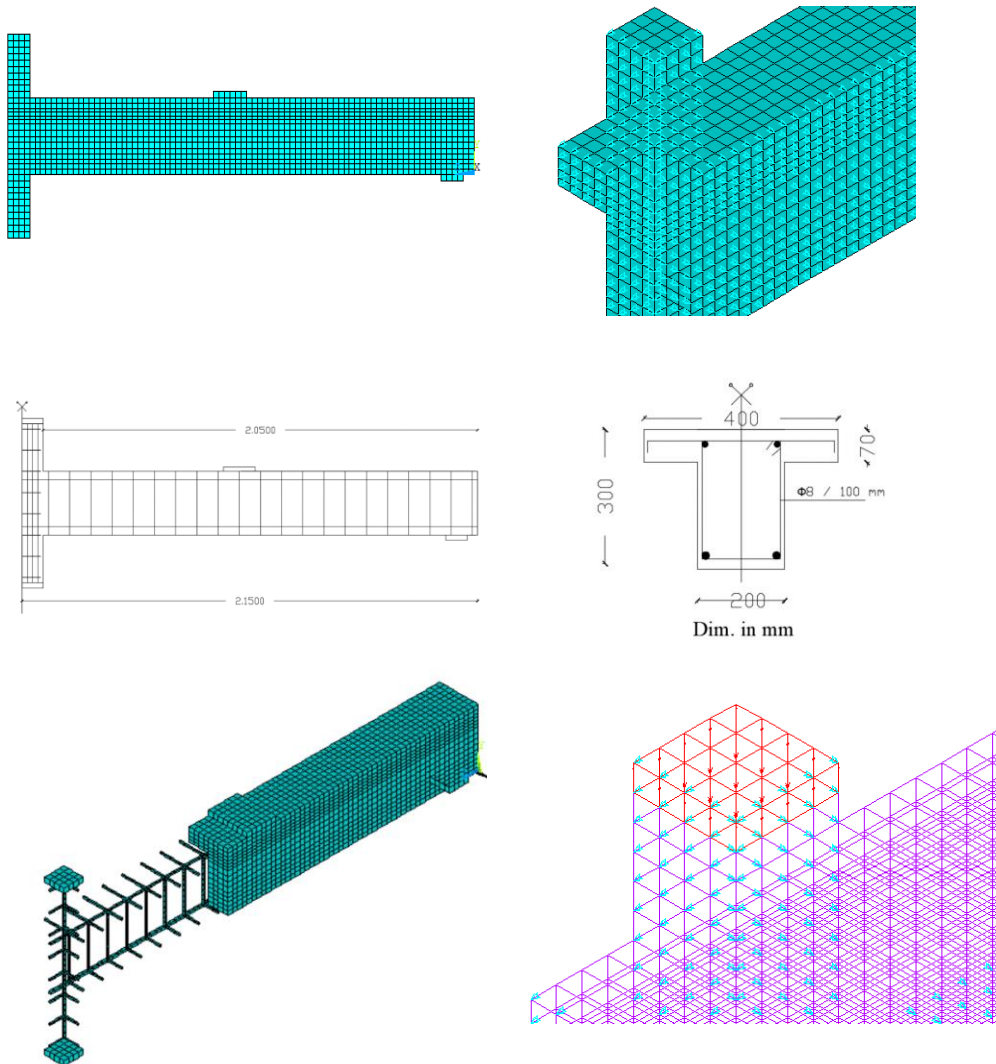
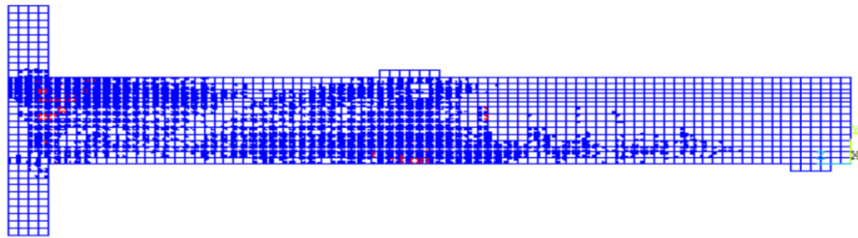


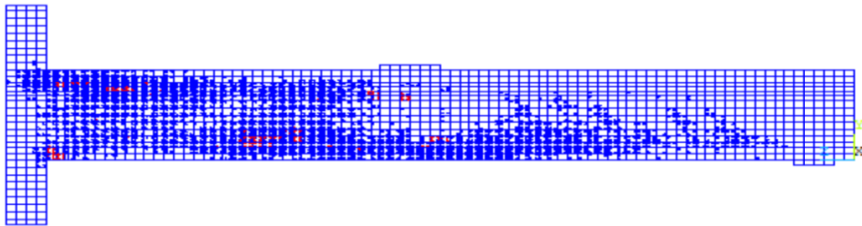
Figure 18: Symmetry axes and boundary conditions.

In order to have a minimal impact on the results and simulate the behavior of the tested beams with the highest possible precision, the size of the mesh used in the model was carefully selected. In order to determine the impact of mesh size on the finite element effects, a preliminary study was performed. In a variety of trials, numerous mesh sizes varying from 75 to 15 mm were used. The coarse mesh with a larger element size was found to show inappropriate conversion problems, leading to premature model failure, in addition to a major difference in the expected performance. This is because, when omitted from the global

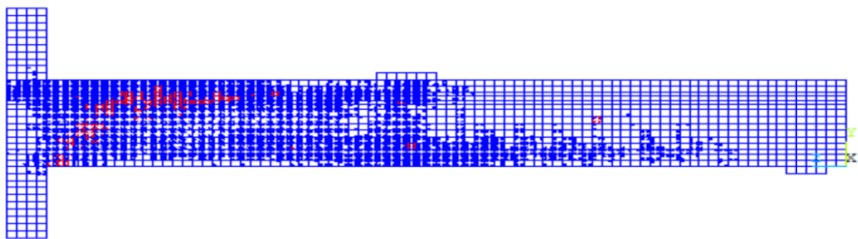
stiffness matrix, cracked elements in coarse mesh cause issues. The use of smaller mesh sizes improved the model's accuracy and decreased the gap in performance, but it required a greater number of nodes. Using smaller mesh sizes, the accuracy of the finite element model converged with a difference of as low as 0.05 percent between 25 mm and 15 mm. In the model, a 3D mesh size of 25 mm was adopted to save computing time. In finite element analysis, the overall applied load is separated into a sequence of load steps to take into consideration the influence of non-linearity. A particular load increment in a certain direction is allocated to each load step.



(a) Beam (BS)

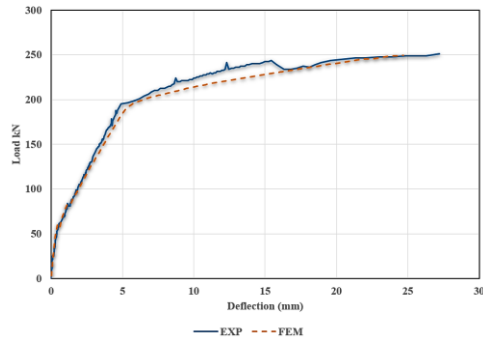


(b) Beam (BH)

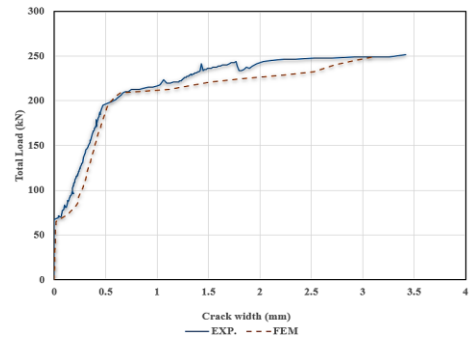


(c) Beam (BCH)

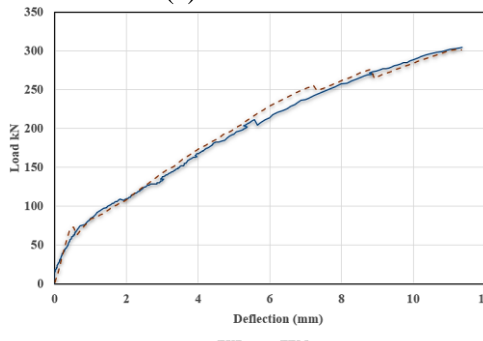
Figure 19: FE mode of failure for representative samples of test beams.



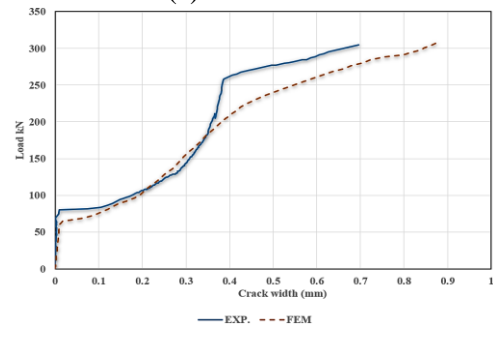
(a) Beam BS



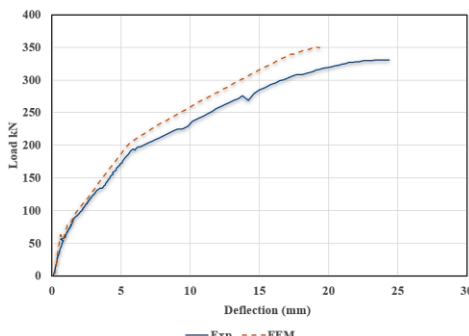
(a) Beam BS



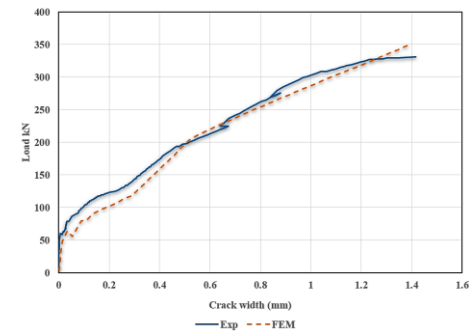
(b) Beam BH



(b) Beam BH



(c) Beam BCH



(c) Beam BCH

Figure 20: Load versus mid-span deflection of tested beams

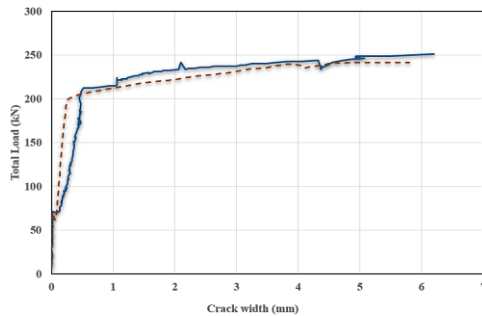
Figure 21: Total applied load versus flexural crack width at the hogging region

5.3 Finite element results and discussion

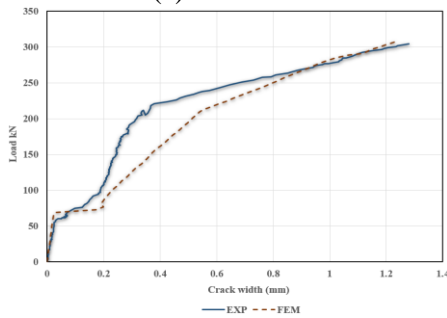
The FEA was able to simulate with fair precision the behavior of the tested specimens, and, despite the difficulties of convergence in the program solution, it was able to predict the post-failure behavior of concrete once failure started.

5.3.1 Modes of failure

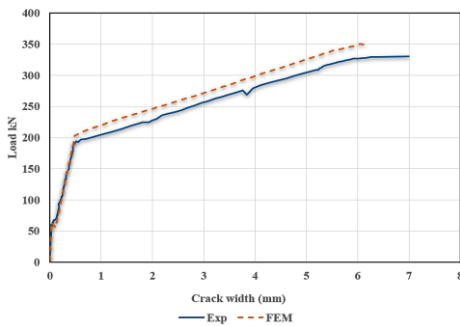
Figure (19) displays the failure modes for test beam samples as observed from the post-processing program FE analysis. It is noted that the modes of failure predicted from the FE study agree very well with the experimental results .



(a) Beam BS

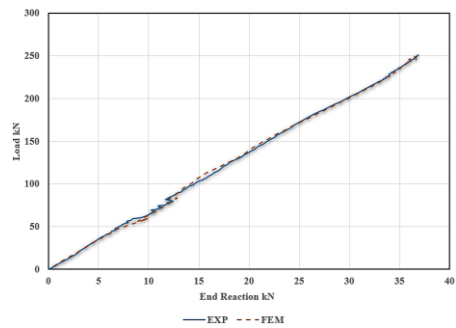


(b) Beam BH

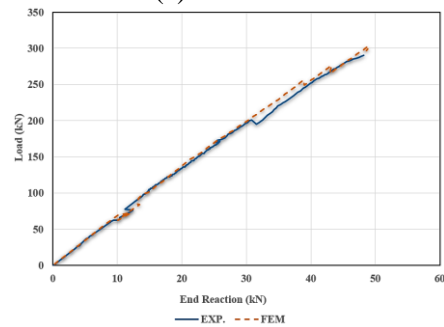


(c) Beam BCH

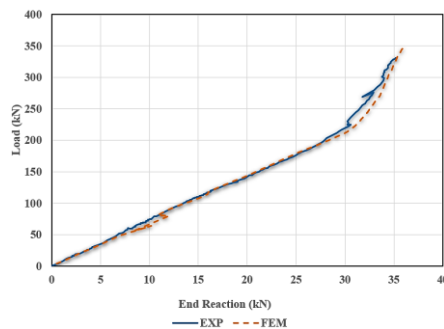
Fig. 22. Total applied load versus flexural crack width at the sagging region



(a) Beam BS



(b) Beam BH



(c) Beam BCH

Fig. 23. Load versus end reactions of beams

From the study, it was found that, like the experimental observations, after the formation of wide flexural cracks in the maximum moment regions, the beam BS failed due to concrete crushing. Because of the yielding of the steel bars at the critical sections followed by diagonal shear cracks at the ultimate load, the hybrid beam BH failed, and about the beam BCH, the failure mode was yielding of the main steel reinforcement at the sagging region followed by a diagonal crack through the beam thickness beside the central loaded column.

Figure (20) shows a comparison between the load-deflection behavior of beams BS, BH, and BCH obtained experimentally and to those obtained using FE analysis. It can be shown that the FEA was able to display a similar reaction to the tested beams. The drop of stiffness after cracking as well as the effect of steel yielding before failure was expected by the models with a suitable accuracy. As seen in Table 7, maximum deviation of 1.1% was found for the numerical results for different load carrying capacities for all tested beams.

Table 7: Comparison between the Experimental and FEA results at yield and ultimate loads.

Beam specimen	Yielding load at hogging region (kN)			Yielding load at sagging region (kN)			Ultimate load (kN)		
	Exp.	FEA	Exp./FEA	Exp.	FEA	Exp./FEA	Exp.	FEA	Exp./FEA
BS	195	185	1.05	202	196	1.03	251.25	249	1.01
BH	208	202	1.03	222	221	1.0	304.5	302	1.01
BCH	—	—	—	221.8	225	0.99	330.8	350	0.95
average	—	—	1.04	—	—	1.01	—	—	0.99

Figures (21 and 22) show the load-crack width at the critical sections for the beams. The FE analysis reasonably predicts the experimental behavior of the crack width of the different beams. The predicted strains by ANSYS were within 7% difference from experimental results. The FE model for beam BH experienced clear difference behavior after the cracking load until the yield load as shown in figure. Comparisons between the experimental and FEA results at different crack width values are shown in Tables (8 and 9). The results were obtained by measuring the width of cracks at the hogging region with a distance 200 mm from the central support and at an 150 mm under the point load at the sagging region as it was experimentally measured.

Table 8: Comparison between the experimental results and the FEA at different crack width value at the hogging region.

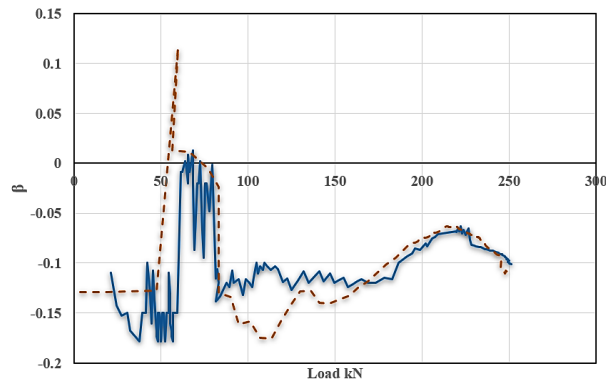
Crack width mm.	BS			BH			BCH		
	Exp.	FEA	Exp./FEA	Exp.	FEA	Exp./FEA	Exp.	FEA	Exp./FEA
0.1	81.3	72	1.13	84	77	1.09	102.5	81	1.27
0.2	111.3	85	1.31	106	105	1.01	123.5	103	1.2
0.3	141.5	113	1.25	144	157	0.92	144.4	124	1.16
0.4	171	156	1.1	264	212	1.25	176	164	1.07
0.5	197	189	1.04	277	240	1.15	198	197	1.01
0.6	202	204	0.99	292	264	1.11	214	222	0.96
average	-----	-----	1.14	-----	-----	1.09	-----	-----	1.11

Table 9: Comparison between the experimental results and the FEA at different crack width value at the hogging region.

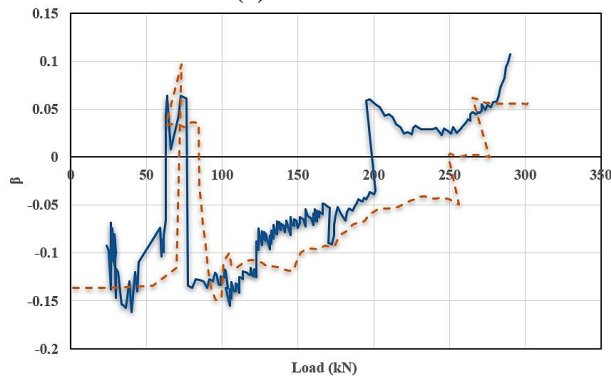
Crack width mm.	BS			BH			BCH		
	Exp.	FEA	Exp./FEA	Exp.	FEA	Exp./FEA	Exp.	FEA	Exp./FEA
0.1	71	85	0.84	75	70	1.07	68.3	64	1.07
0.2	91	150	0.61	107.6	88.7	1.21	99.8	97	1.03
0.3	130	200.7	0.65	195	129	1.51	134	130	1.03
0.4	161	204	0.79	223	165	1.35	165.4	174	0.95
0.5	212.5	206	1.03	233	197	1.18	194.2	203	0.96
0.6	213	207	1.03	243	220.4	1.1	196.9	208	0.95
average	-----	-----	0.83	-----	-----	1.24	-----	-----	1.0

Since the challenge is statically indeterminate, to predict the model's ability to redistribute bending moments, the expected and experimental end reactions were compared. For both experimental and ANSYS results, the relation between total applied load and end reactions of different beams is shown in figure (23). Again, between the predicted and experimental results, a reasonable agreement can be seen. These reaction results from ANSYS were used to determine the bending moment with different applied loads on the middle support section. For the measurement of the moment redistribution percentage at middle support, the bending moments predicted by ANSYS are compared to the elastic bending moment at the same critical section ($0.188 P\ell$, where P is the applied load and ℓ is the beam span). The model has been able to redistribute moments of bending between critical sections. Figure (24) show the relationship between the moment redistribution at the hogging region and the total load. It can be shown that right after cracking, the finite element model showed substantial redistribution of moments. The

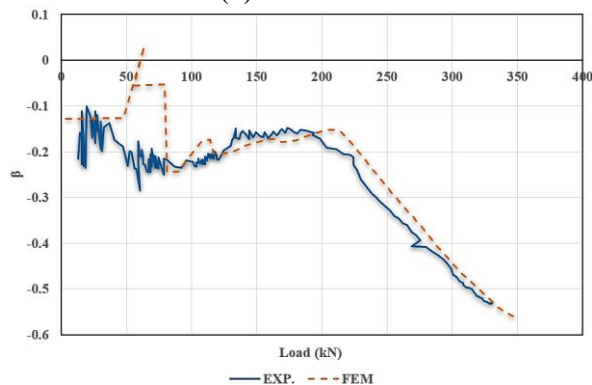
expected moment redistribution was within a range of 20% deviation from experimental results.



(a) Beam BS



(b) Beam BH



(c) Beam BCH

Figure 24: Load versus moment redistributions at middle support.

6. Conclusions

To research the flexural behavior of reinforced concrete continuous beams, experimental work was conducted on three large-scale RC continuous T-beams. In both critical regions, the tested beams were reinforced with either CFRP bars or combination CFRP/steel bars to examine the general behavior of the tested beams before failure. Moreover, the ability of the tested beams to redistribute the internal forces between central support and mid-span regions under the vertical loads. The following conclusions can be established based on the test results and the comparisons between the test beams provided in advance in this study:

- The hybrid-reinforced beam showed stable and better post-yield stiffness values compared with the beam reinforced with steel only with identical initial rigidity values of the RC-continuous beams.
- Mode of failure depends deeply on the type of the main reinforcement in both critical areas, where reinforcement with CFRP bars displayed less deflections and narrower crack widths at service load.
- The moment redistribution ratio values change according to the type of the main reinforcement at both critical sections. Reinforcing with CFRP bars at the hogging region shows a ductile failure and ultimate load capacity more than that was reinforced with hybrid bars at both regions.
- Reinforcement with CFRP bars at the hogging region helped to control the crack width and the flexural rigidity, which helped to redistribute the internal force to the hogging region. This will help to increase the sagging reinforcement area without respectable increase in the moment redistribution ratio and with significant improvement in both flexural rigidity and moment capacity.
- With the available moment redistribution, the defined FE model was capable of predicting load-deflection behavior with reasonable accuracy. The FEA should also be used to perform a parametric analysis to expand the range of the parameters studied to enhance knowledge of their effect on continuous RC T-beams reinforced with hybrid reinforcement.

References

- [1] Yang Y, Sun ZY, Wu G., Cao DF, Pan D. Experimental study of concrete beams reinforced with hybrid bars (SFCBs and BFRP bars). *Material and Structures*, 53, 77 (2020). <https://doi.org/10.1617/s11527-020-01514-8>
- [2] Kocaoz S, Samaranayake VA, Nanni A. Tensile characterization of glass FRP bars. *Composites: Part B: Engineering*, 36, pp. 127–34, 2005.
- [3] El-Mogy M, El-Ragaby A, El-Salakawy E. Behavior of Continuous Concrete Beams Reinforced with FRP Bars. In: Ye L., Feng P., Yue Q. (eds) *Advances in FRP Composites in Civil Engineering*. Springer, Berlin, Heidelberg, 2011. https://doi.org/10.1007/978-3-642-17487-2_60
- [4] Kara IF, Ashour AF, Dundar C. Deflection of concrete structures reinforced with FRP bars. *Composites: Part B Engineering*, 44, pp. 375–84, 2013.
- [5] Ge W, Zhang J, Cao D, Tu Y. Flexural behavior of hybrid concrete beams reinforced with BFRP bars and steel bars. *Construction and Building Materials*, 87, pp. 28–37, 2015.
- [6] Nanni A, Henneke MJ, Okamoto T. Tensile properties of hybrid rods for concrete reinforcement. *Construction and Building Materials*, 8(1), pp. 27–34, 1994.
- [7] Tepfers R, Tamužs V, Apinis R, Vilks U, Modniks J. Ductility of nonmetallic hybrid fiber composite reinforcement for concrete. *Mechanics of Composite Materials*, 32(2), pp. 113–21, 1996.
- [8] Cheung MM, Tsang TK. Behaviour of concrete beams reinforced with hybrid FRP composite rebar. *Advances in Structural Engineering*, 13(1), pp. 81–93, 2010.
- [9] Behnam B, Eamon C. Analysis of alternative ductile fiber-reinforced polymer reinforcing bar concepts. *Journal of Composite Materials*, 48(6), pp. 723–33, 2014.
- [10] Said, M, Shanour, AS, Mustafa, TS, Abdel-Kareem, AH, Khalila, MM Experimental flexural performance of concrete beams reinforced with an innovative hybrid bars. *Engineering Structures* 226, 111348, 2021.
- [11] Lau D, Pam HJ. Experimental study of hybrid FRP reinforced concrete beams. *Engineering Structures*, 32(12), pp. 3857–65, 2020.
- [12] Safan MA. Flexural behavior and design of steel-GFRP reinforced concrete beams. *ACI Materials Journal*, 110(6), pp.677–86, 2013.
- [13] El Refai A, Abed F, Al-Rahmani A. Structural performance and serviceability of concrete beams reinforced with hybrid (GFRP and steel) bars. *Construction and Building Materials*, 96, pp. 518–29, 2015.
- [14] Mohamed EA, Ashour AF Flexural performance of hybrid GFRP-Steel reinforced concrete continuous beams, *Composites Part B: Engineering*, 154, pp. 321-336, 2018.
- [15] Xingyu, G, Yiqing, D, Jiwang, J. Flexural behavior investigation of steel-GFRP hybrid-reinforced concrete beams based on experimental and numerical methods. *Engineering Structures*, 206, 110117, 2020.
- [16] Diab HM, Abdelaleem T, Rashwan MM. Moment redistribution and flexural performance of RC continuous T-beams strengthened with NSM FRP or steel bars. *Structures*, 28, pp. 1516– 38, 2020.

- [17] Diab HM., Abdelaleem T, Rashwan MM. experimental investigation of Moment redistribution in RC continuous beams with T-cross section considering central loaded support. *International Journal of Civil Engineering and Technology (IJCET)*, 11(7), pp. 114-130, 2020.
- [18] BD 2004. Code of practice for structural use of concrete 2004. Buildings Department (BD), The Government of the Hong Kong Special Administration Region, 180 p., 2004
- [19] ACI Committee 318. Building Code Requirements for Structural Concrete and Commentary (ACI 318-19), 2019.
- [20] American Concrete Institute (ACI). Guide for the design and construction of concrete reinforced with FRP bars vol. 440. 1R-15, Farmington Hills, Mich: ACI; 2015.
- [21] Qin R, Zhou A, Lau D. Effect of reinforcement ratio on the flexural performance of hybrid FRP reinforced concrete beams. *Composites Part: B Engineering*, 108, pp. 200-209, 2017.
- [22] Abdelaleem T, Rashwan M, Diab HM. New aspects about the effect of strengthening type and technique on the moment redistribution of RC continuous beams (Experimental and Numerical Study) [Ph.D. thesis]. Egypt: Assiut University, 2020.
- [23] Sun ZY, Yang Y, Qin WH, Ren ST, Wu G. Experimental study on flexural behavior of concrete beams reinforced by steel-fiber reinforced polymer composite bars. *Journal of Reinforced Plastics and Composites*, 31(24), pp. 1737–45, 2012.
- [24] ANSYS Mechanical Enterprise. A finite element computer software and user manual for nonlinear structural analysis. Mechanical APDL Release 18.1 UP20170403.
- [25] Kachlakev D, Miller T, Yim S, Chansawat K, Potisuk T. Finite element modeling of reinforced concrete structures strengthened with FRP laminates. Final Report SPR-316, Oregon Department of Transportation, Salem, Oregon, 2001.
- [26] Büyükkaragöz A. Finite element analysis of the beam strengthened with prefabricated reinforced concrete plate. *Scientific Research and Essays*, 5(6), pp. 533- 44, 2010.
- [27] Egyptian Code of Practice for Design and Construction of Concrete Structures ECP 203-٢٠١٧, 2017.
- [28] Quintero-Febres CG, Wight JK. Experimental study of reinforced concrete interior wide beam–column connections subjected to lateral loading. *ACI Structural Journal*, 98, pp. 572–82, 2001.

سلوك الانحناء للكمرات الخرسانية المستمرة وذات قطاع على شكل حرف (T) والمسلحة بتسليح هجين من قضبان البوليمرات المسلحة بألياف الكربون (CFRP) وصلب التسليح (دراسة عملية ونظرية)

الملخص العربي:

يقدم هذا البحث دراسة عملية ونظرية لسلوك الكمرات الخرسانية المستمرة وذات قطاع على شكل حرف (T) والمسلحة بتسليح هجين من قضبان البوليمرات المسلحة بألياف الكربون (CFRP) وصلب التسليح في مناطق أقصى العزوم الموجبة والسالبة (Sagging & Hogging). تم اعداد برنامج عملي يتكون من ثلاث كمرات مستمرة وذلك لدراسة المتغيرات الآتية: (1) نوع مادة التسليح في القطاع، (2) نوع التسليح في منطقة أقصى عزم موجب وأقصى عزم سالب، (3) مقدار وسلوك إعادة توزيع العزوم بين القطاعات الحرجة. تم تصميم وتسليح الكمرات المرجعية باستخدام أسياخ صلب التسليح لكي يحدث الانهيار في مناطق أقصى عزم. تم تسليح الكمرات الثانية باستخدام تسليح هجين في مناطق أقصى عزم موجبة وسالبة. وأيضاً تم تسليح الكمرات الثالثة بقضبان البوليمرات المسلحة بألياف الكربون (CFRP) في منطقة أقصى عزم سالب فقط (Hogging) وبأسياخ صلب التسليح في منطقة العزوم الموجب (Sagging). تم تصميم جميع القطاعات الحرجة في الكمرات المختبرة لتكون لها نفس الصلابة المحورية (Axial stiffness) لقضبان التسليح. أظهرت النتائج العملية أن نسبة إعادة التوزيع للعزوم وانماط الانهيار يعتمدان على نوع أسياخ التسليح واستخدام التسليح الهجين في كلا القطاعين الحرجين ساعد في التحكم في حدود التشغيل طبقاً للاكواد التصميمية. تقدم هذه الدراسة أيضاً نموذجاً عددياً ثلاثي الأبعاد للتنبؤا بسلوك الكمرات المستمرة والمسلحة بتسليح هجين وذلك باستخدام برنامج العناصر المحدود "ANSYS". واثبتت النتائج التي تم الحصول عليها من هذا النموذج العددي تقارباً الى حد كبير مع النتائج التي الحصول عليها معملياً.